

Forecast analysis and focal plane optimization for a multi-frequency CMB B -modes polarization experiment: the case of LSPE

R. Mainini,^a M. Gervasi,^b M. Zannoni,^b L. Lamagna^c

^aPhysics Department, University of Milano–Bicocca,
Piazza della Scienza 3, I20126, Milano, Italy

^bPhysics Department, University of Milano–Bicocca and INFN - Milano–Bicocca,
Piazza della Scienza 3, I20126, Milano, Italy

^cPhysics Department, Sapienza University of Rome,
Piazzale Aldo Moro 5, I00185, Roma, Italy

E-mail: roberto.mainini@mib.infn.it

Abstract. We present an optimization scheme for the focal plane of a multi-frequency CMB B -modes experiment with a fixed number of detectors and apply it to the specific case of LSPE experiment. Optimal focal planes are identified on the ground of different figures of merit defined in terms of the forecasted uncertainty σ_r on the tensor-to-scalar ratio r and the expected map variance from foreground and instrumental noise residuals. We then perform a forecast analysis in order to assess the precision achievable in B -modes measurements.

Contents

1	Introduction	1
2	Fisher Matrix forecasts	3
3	Focal plane optimization	6
3.1	High frequencies	6
3.1.1	Reducing the detector noise	7
3.1.2	Frequency channel correlations	8
3.2	High+Low frequencies	9
3.3	Including E -modes	11
4	Conclusions	13
A	Foreground removal	15
B	Foreground models	17
C	Instrumental noise	18
D	Angular power spectra covariance matrix	19

1 Introduction

Detecting B -modes of polarization represents a challenge for the next generation of CMB experiments. The importance of such measurements regards the intimate connection between B -modes and the physics of primordial Universe. As matter of fact B -modes were originated from the stochastic background of gravitational waves expected from a wide class of inflationary models. The detection of B -modes at large angular scales, in addition to being the definitive confirmation of the inflation theory, offers the unique opportunity to probe energy scales as high as $3.3 \times 10^{16} r^{\frac{1}{4}}$ GeV, out of the target of any particle accelerator (here and in the following r is the tensor-to-scalar ratio at the pivot scale $k_* = 0.05 \text{ Mpc}^{-1}$ which parametrizes the amplitude of the primordial gravitational wave signature in the CMB polarization).

A reliable detection of B -modes is however a difficult task. In addition to being extremely tiny, their signal is buried in the diffuse galactic foregrounds, namely the polarized synchrotron and thermal dust emissions, requiring technologically advanced instruments, utmost sensitivity, unprecedented control of systematic effects, as well as a wide frequency coverage in order to disentangle or reduce foreground contaminations. The strongest constraints to date on the tensor-to-scalar ratio r are provided by the analysis in [1] yielding $r < 0.07$ at 95 % confidence level.

To further constrain the value of r or, hopefully, achieve the detection of B -modes, ground based or balloon-borne experiments are being performed or planned. The LSPE (Large Scale Polarization Explorer) mission, supported by the Italian Space Agency (ASI), is designed for this endeavor. It consists of two instruments composed by array of detectors: the Short Wavelength Instrument for the Polarization Explorer (SWIPE) and the STRatospheric Italian Polarimeter (STRIP), observing in different frequency ranges the same sky fraction

($\sim 20 - 25\%$). SWIPE is a balloon-borne bolometric instrument which will operate during the Arctic night (at latitude around 78 degree and for around 15 days) at three frequency bands centered at 140, 220 and 240 GHz, with an angular resolution of about 1.5 degrees. STRIP is the ground-based, low frequency module of LSPE. It consists of an array of coherent polarimeters which will survey the sky from Teide observatory at Tenerife for 1–2 years in frequency bands centered at 43 and possibly 90 GHz, with an angular resolution of about 0.5 degrees. Further details on instruments characteristics and informations on LSPE experiment can be found in Table 4 and [2–7]. In its latest proposed configuration, the focal plane of STRIP is composed by 49 detectors at 43 GHz, plus 4/6 detectors at 90 GHz mainly used as monitors of atmospheric emission, while SWIPE includes two focal planes each consisting of 3 frequency channels: 140, 220 and 240 GHz with 55, 56 and 52 detectors respectively, for a total of $163 \times 2 = 326$ detectors. At this time, due to instrument’s geometry and some technological details, this solution is the favorite one, although there is still room for slight changes.

The aim of this note is the investigation of the optimal focal plane configurations of the LSPE experiment for primordial B -modes measurements. In the following we therefore consider deviations from the above configuration (also considering different combination of frequencies) in order to check whether the performance in constraining r can be improved. Our criteria to identify the optimal configurations will be the values of the forecasted uncertainty σ_r on the tensor-to-scalar ratio r and/or the expected map variance from foreground and instrumental noise residuals. We will see that configurations yielding the lowest variance do not necessarily minimize the uncertainty on r . A similar but more sophisticated analysis was performed in [8] and applied to CMBpol and CORE satellite experiments while a detailed investigation of the capability of LSPE (also in combination with other CMB experiments) to constrain inflationary parameters will be performed in [9].

Although specific for LSPE, our results could nevertheless be of interest for the design of similar experiments. In our analysis we did not consider several sources of systematics not so trivial to be taken into account, such as the non-circularity of the beam pattern or phase-angle uncertainty which can introduce a leakage into detected B -modes. Regarding STRIP we did not consider systematic effects coming from the atmospheric fluctuations or long term instabilities, in particular, as suggested in literature [10–12], we neglect possible residual polarization of the atmospheric emission.

The plan of the paper is as follows: in Section 2 we describe the Fisher Matrix based method adopted to forecast the achievable precision on r while in Section 3 our approach to focal plane optimization and our findings are presented. Results are first given by considering only the high frequency instruments SWIPE and B -modes measurements. We then consider the combination SWIPE+STRIP and include the E -modes in the analysis. Effects of detector noise and frequency channel correlations on results are also discussed. Finally, Section 4 is devoted to conclusions. Appendices collect some material needed to implement our analysis: in Appendix A we describe the adopted method for estimating galactic foreground (and instrumental noise) residuals to be included in the Fisher Matrix forecasting analysis. Foregrounds are modeled according to recent findings of Planck collaboration and detailed in Appendix B while characteristics of LSPE instruments are summarized in Appendix C. The polarization angular power spectra covariance matrix entering the Fisher Matrix is given in Appendix D.

2 Fisher Matrix forecasts

In order to estimate the precision achievable on r we make use of the Fisher Matrix (FM) approach. Let C_l^X and R_l^X ($X = E, B$) denote the angular power spectra of CMB polarization and residual non-cosmic signal (foregrounds and instrumental noise) respectively. We then define the binned power spectra in multipole bands b of width Δl :

$$D_b^X = \frac{1}{\Delta l} \sum_{l \in b} D_l^X \quad (2.1)$$

where

$$D_l^X = \frac{l(l+1)}{2\pi} (C_l^X + R_l^X) \quad (2.2)$$

The Fisher Matrix then reads:

$$\begin{aligned} F_{ij} &= \sum_X \sum_b F_{ij,b}^X + \frac{\delta_{ij}}{\sigma_P^2(p_i)} \\ &= \sum_X \sum_b \frac{\partial D_b^X}{\partial p_i} [\mathbf{D}_b^{-1}]_{XX} \frac{\partial D_b^X}{\partial p_j} + \frac{\delta_{ij}}{\sigma_P^2(p_i)} \end{aligned} \quad (2.3)$$

Here $\sigma_P(p_i)$ denotes a possible Gaussian prior on the model parameter p_i and the derivatives are evaluated at the fiducial model values. The covariance matrix of the binned power spectra, \mathbf{D}_b , is given in Appendix D. The inverse of FM then gives the covariance matrix C_{ij} of the model parameters, the diagonal elements of which represent the lowest variance $\sigma^2(p_i)$ one can achieve on the parameter p_i .

The limited sky fraction observed by LSPE ($f_{sky} \simeq 0.2$) places a limit on the minimum resolution Δ_l of the angular power spectra under which different multipoles become correlated. This is approximately given by $\Delta_l = \pi/\Theta$ (Θ^2 being the survey area), thus, in our analysis we consider multipole bins of width $\Delta_l = 3$. Since LSPE will measure polarization, the only relevant foregrounds included in the analysis are polarized dust and synchrotron emissions which we model according to the recent findings of the Planck collaboration (see Appendix B).

In order to perform our FM analysis we need to estimate the residuals R_l^X , arising after some foreground (and instrumental noise) cleaning procedure. To this aim, here, we adopt the method proposed by [13] and detailed in Appendix A.

As a base cosmological model we assume a flat Λ CDM cosmology with tensor perturbations described by the following seven parameters:

$$\{\Omega_b h^2, \Omega_c h^2, \theta, \tau, n_s, \ln(10^{10} A_s), r\}$$

where Ω_b are Ω_c are the baryon and cold dark matter density parameters respectively, h is the dimensionless Hubble parameter, θ is the angle subtended by the sound horizon at recombination, τ is the optical depth to reionization, n_s is the scalar spectral index, A_s is the amplitude of scalar fluctuations at a pivot scale $k^* = 0.05 \text{ Mpc}^{-1}$ and r is the tensor to scalar ratio. Fiducial values of the six standard cosmological parameters $\{\Omega_b h^2, \Omega_c h^2, \theta, \tau, n_s, \ln(10^{10} A_s)\}$ are set to the best fit values estimated by Planck Collaboration 2015 [14] (Planck $TT, EE, TE + \text{low}P$ data) while we assume a fiducial $r = 0.05$ all through the paper with the exception of section 3.3 where the range $0.01 \leq r \leq 0.1$ is considered.

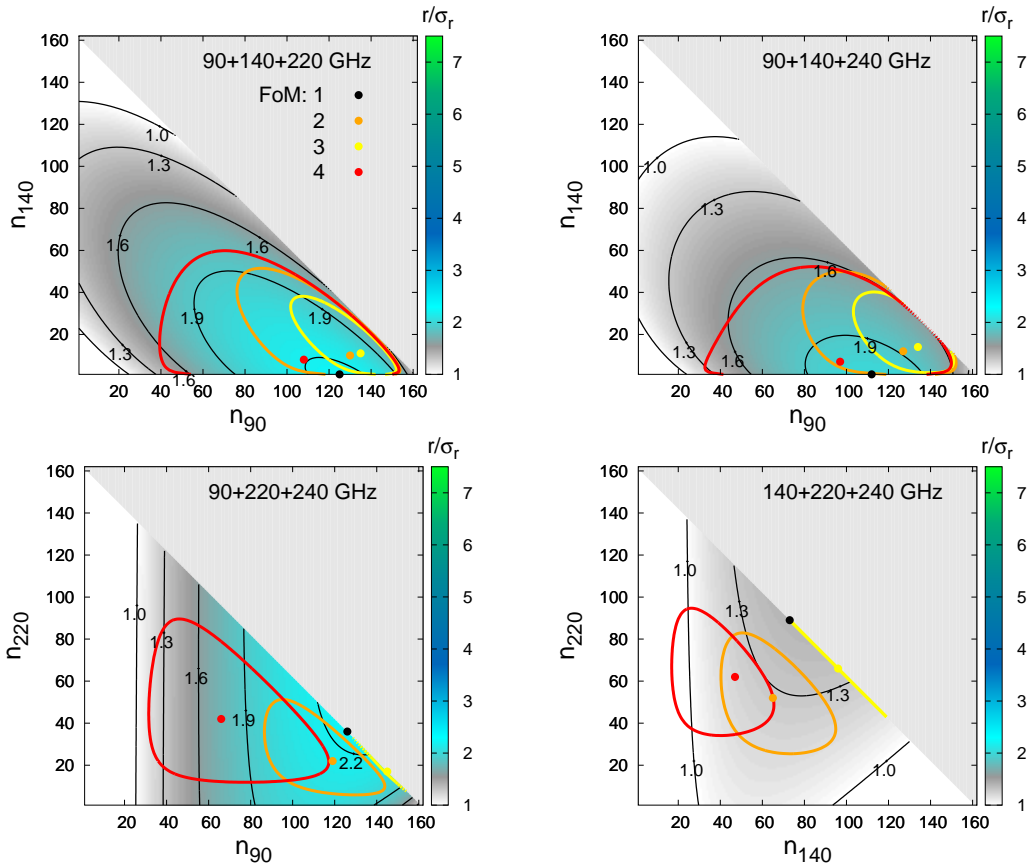


Figure 1. Contour levels for $r/\sigma_r \geq 1$ in steps of 0.3 for different combinations of SWIPE frequency channels. Black, orange, yellow and red dots indicate configurations satisfying FoM 1, 2, 3 and 4 respectively (see text). Orange, red and yellow curves surround the configurations for which the variances, σ_{tot}^2 , σ_{for}^2 and σ_{det}^2 , deviate by no more than 5% from their minimum values.

Since LSPE measurements will be limited to the first ~ 140 multipoles of polarization spectra, strong constraints are expected only on r and τ . Therefore, when applying the FM approach all the cosmological parameters will be kept fixed to their fiducial values except for:

- i) r if only B -modes are included in the analysis,
- ii) r , τ and $\ln(10^{10} A_s)$ (the latter being strongly correlated with τ) if both E - and B -modes are included.

Moreover, amplitudes $\mathcal{A}_{D(S)}^X$ and spectral indices $\beta_{D(S)}$ of dust (D) and synchrotron (S) spectra will be included in the analysis as nuisance parameters and marginalized over. Foreground models and adopted priors are detailed in Appendix B while Appendix C describes the characteristics of LSPE instruments.

It is worth noticing that the simplified procedure here adopted does not address a number of issues. For partial sky experiments the number of modes of multipole l available for the analysis decreases with the sky coverage. As usual, to capture this effect we simply assume that the number of independent modes of a given multipole is approximately reduced by a

90+140+220 GHz							
FoM	r/σ_r	$\sigma_{\text{tot}}^2/\mu\text{K}^2$	$\sigma_{\text{det}}^2/\mu\text{K}^2$	$\sigma_{\text{for}}^2/\mu\text{K}^2$	n_{90}	n_{140}	n_{220}
1	2.2400	0.0814	0.0234	0.0580	125	1	37
2	2.1325	0.0783	0.0213	0.0570	130	10	23
3	2.0569	0.0784	0.0211	0.0573	135	11	17
4	2.1937	0.0802	0.0235	0.0566	108	8	47

90+140+240 GHz							
FoM	r/σ_r	$\sigma_{\text{tot}}^2/\mu\text{K}^2$	$\sigma_{\text{det}}^2/\mu\text{K}^2$	$\sigma_{\text{for}}^2/\mu\text{K}^2$	n_{90}	n_{140}	n_{240}
1	2.0322	0.0844	0.0263	0.0581	112	1	50
2	1.8790	0.0797	0.0227	0.0570	127	12	24
3	1.7898	0.0800	0.0225	0.0575	134	14	15
4	1.9778	0.0828	0.0265	0.0564	97	7	59

90+220+240 GHz							
FoM	r/σ_r	$\sigma_{\text{tot}}^2/\mu\text{K}^2$	$\sigma_{\text{det}}^2/\mu\text{K}^2$	$\sigma_{\text{for}}^2/\mu\text{K}^2$	n_{90}	n_{220}	n_{240}
1	2.2368	0.0888	0.0257	0.0632	126	36	1
2	2.1636	0.0763	0.0276	0.0487	119	22	22
3	2.0991	0.0885	0.0244	0.0641	145	17	1
4	1.7552	0.0873	0.0411	0.0462	66	42	55

140+220+240 GHz							
FoM	r/σ_r	$\sigma_{\text{tot}}^2/\mu\text{K}^2$	$\sigma_{\text{det}}^2/\mu\text{K}^2$	$\sigma_{\text{for}}^2/\mu\text{K}^2$	n_{140}	n_{220}	n_{240}
1	1.3980	0.1662	0.0400	0.1262	73	89	1
2	1.2845	0.1159	0.0509	0.0650	65	52	46
3	1.3371	0.1657	0.0384	0.1273	96	66	1
4	1.1202	0.1263	0.0644	0.0619	34	63	66

Table 1. Values of r/σ_r , variances and the number of detectors corresponding to the configurations satisfying FoM 1, 2, 3 and 4 for different combinations of SWIPE frequency channels.

factor of f_{sky} , i.e. $(2l+1) \rightarrow (2l+1)f_{sky}$. This is taken into account in the definition of \mathbf{D}_b . However, in case of polarization, partial sky coverage causes a leakage of E -modes into B -modes (neglected in our analysis) which can alter the scaling with f_{sky} [15] other than add complications to the detection of primordial gravitational waves. Another issue concerns the B -modes signal induced by weak lensing which is a limiting factor in measuring B -modes of primordial origin. We assume no removal of lensing contamination and treat it as a Gaussian noise for simplicity. However, lensing is not important at low multipoles if the tensor to scalar ratio is large or when the residual noise is larger than the lensing signal. For simplicity we also assume foregrounds to have a Gaussian probability distribution although, generally, they

do not. We also neglect correlations among galactic dust and synchrotron recently measured by [16, 17].

3 Focal plane optimization

3.1 High frequencies

In this Section we only consider the high frequency instrument (SWIPE) and B -modes measurements so that the set of parameters to vary in FM analysis is $\mathbf{p} = \{r, \mathcal{A}_S^B, \mathcal{A}_D^B, \beta_S, \beta_D\}$.

We assume each of the two (identical) focal planes to consist of 3 frequency channels ($\nu_i, i = 1, 2, 3$) each with n_{ν_i} detectors for a total of $n_{tot} = 163$ detectors. Further, all the detectors are supposed to have the same size so that different combinations occupy the same area.

Next we consider all the configurations obtained by varying the n_{ν_i} 's such that $n_{\nu_1} + n_{\nu_2} + n_{\nu_3} = 163$ and apply the cleaning procedure of Appendix A and the FM formalism to each of them. We then define the following Figures of Merit (FoM):

FoM 1 maximum signal to noise ratio r/σ_r

FoM 2 minimum variance, σ_{tot}^2 , from residual foregrounds and detector noise

FoM 3 minimum variance, σ_{det}^2 , from residual detector noise

FoM 4 minimum variance, σ_{for}^2 , from residual foregrounds

where:

$$\sigma_{tot}^2 = \sum_b R_b^B \sum_{l \in b} \frac{2l+1}{4\pi} W_l$$

(R_b^B is the binned angular power spectrum of residual foregrounds and detector noise, W_l is the beam window function) and similar expressions hold for σ_{for}^2 and σ_{det}^2 . Finally, we select and compare the configurations that satisfy the above FoM's.

We start by considering all the combinations of 3 frequencies chosen among 90, 140, 220 and 240 GHz. Results are displayed in Figure 1 which shows: i) contour levels for $r/\sigma_r \geq 1$ in steps of 0.3, ii) configurations satisfying FoM 1, 2, 3 and 4 (black, orange, yellow and red dots respectively; orange, red and yellow curves surround the configurations for which the variances, σ_{tot}^2 , σ_{for}^2 and σ_{det}^2 , deviate by no more than 5% from their minimum values). Table 1 summarizes the values of r/σ_r , the variances and the number of detectors corresponding to the configurations in ii).

We first note that the combination 140 + 220 + 240 GHz provides the worst results. This is due to the absence of the frequency channel at 90 GHz for which foregrounds are minimal and the instrumental noise is low (see Table 4). Indeed, when present, the 90 GHz channel is assigned with the majority of detectors. We also observe that requiring the variance to be minimal does not guarantee the best precision on r , although in some cases differences are only marginal. This can be understood by inspection of Figure 2 where, for illustrative purpose, we consider the cases FoM 1 and FoM 2 for the combination 140 + 220 + 240 GHz. The left panel compares the spectra of residual non-cosmic signal, R_l^B , in the two cases. FoM 2 allows for a better foreground cleaning at low multipoles ($l \lesssim 10$) which results in a lower variance σ_{tot}^2 . Nevertheless, the better precision σ_r ($\simeq 1/\sqrt{F_{rr}}$ for negligible correlations among r and foreground parameters) achievable in the case FoM 1, is to be ascribed to the (slight) lower R_l^B at $l \gtrsim 20$ which makes the inverse covariance matrix \mathbf{D}_b^{-1} to increase. This can be inferred

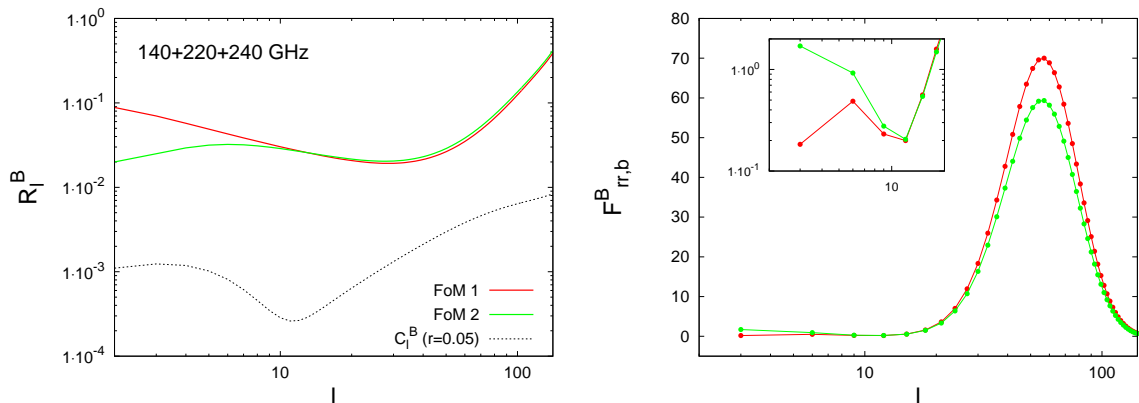


Figure 2. *Left panel:* angular spectra of residual non-cosmic signal in the cases FoM 1 and FoM 2 for the combination SWIPE 140 + 220 + 240 GHz. *Right panel:* contributions to Fisher Matrix in the two cases.

from the right panel of Figure 2 showing that most of the contributions $F_{rr,b}^B \propto \mathbf{D}_b^{-1}$, to the Fisher Matrix come from multipoles in the range $40 \lesssim l \lesssim 80$.

In the following we consider only the combination of frequencies having the best (worst) performance, namely 90 + 140 + 220 GHz (140 + 220 + 240 GHz). Although the 90+220+240 GHz combination performs similarly to 90 + 140 + 220 GHz, we prefer the latter since configurations satisfying our FoM's are quite close each other, all laying in the region with the higher r/σ_r (see Fig. 1).

3.1.1 Reducing the detector noise

In this section we inspect the effect of reducing the instrumental noise. To this aim the sensitivities σ_{pix} of each channel (see Table 4) are simultaneously reduced by a common factor q . Let us first consider the combination 140 + 220 + 240 GHz. Figure 3 illustrates how the configuration's features change when the detector noise is reduced by $q = 0.5, 0.1, 0.05$ while Figure 4 shows the values of r/σ_r and σ_x^2 ($x = \text{tot}, \text{det}, \text{for}$) obtained by the configurations satisfying our FoM's as a function of q in the range $q = 0.01 - 1$.

Focusing first on FoM 1 and Figure 4, we can observe a discontinuity in the behavior of σ_x^2 (black curves) to occur around $q \simeq 0.055$ which corresponds to a transition of the configuration FoM 1 from $\{n_{140}, n_{220}, n_{240}\} \simeq \{67, 95, 1\}$ to $\{37, 73, 53\}$ (see Figure 3, black dots). To understand this behavior, let us remember that most of the contributions to r/σ_r arise from multipoles in the range $l = 40 - 80$ (see section 3.1 and Figure 2) where the detector noise starts to increase above the foreground level. Contributions to r/σ_r are then suppressed by growing noise at larger l . Therefore, in order to maximize r/σ_r , the optimization procedure tends to limit the instrumental noise effect omitting noisier channels, i.e. the 240 GHz channel. On the other hand, as the noise is made smaller, foregrounds become more and more relevant in the full range of multipoles considered so that they should be efficiently removed. To this aim, the 240 GHz channel is also required. Referring to Figure 3, once the noise level decreases sufficiently, a new local maximum for r/σ_r forms around $\{37, 73, 53\}$ becoming absolute for $q < 0.055$. Something similar happens in the case of FoM 3. Around $q \simeq 0.6$ a transition occur from $\{88, 74, 1\}$ to $\{72, 53, 38\}$ causing discontinuities in r/σ_r , σ_{tot}^2 and σ_{for}^2 (yellow

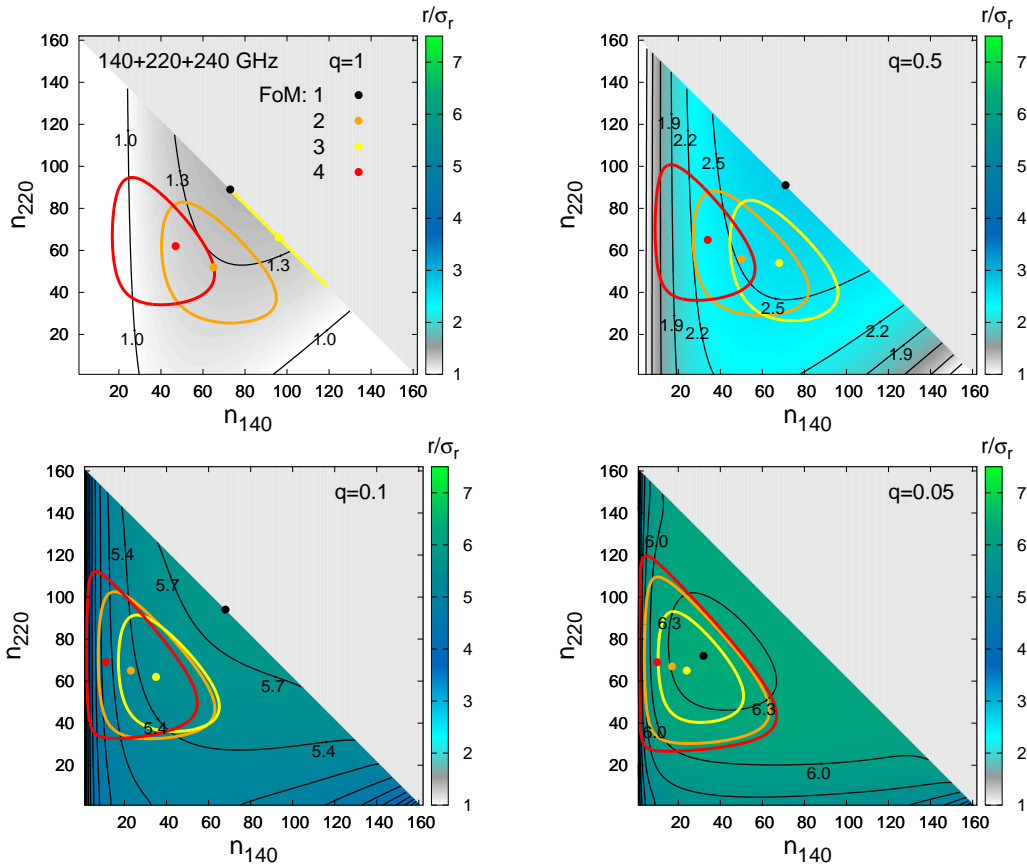


Figure 3. Changes in the features of focal plane configurations for SWIPE 140 + 220 + 240 GHz as the detector noise is reduced by a factor $q = 0.5, 0.1, 0.05$. Lines and colors are like in Figure 1.

line in Figure 4). Figures 5 and 6 are similar to Figures 3 and 4 but for the combination 90 + 140 + 220 GHz.

It is however worth mentioning that in order to improve the detector’s sensitivity, σ_{pix} , a longer observation time, t_{obs} , is required. According to $\sigma_{pix} \propto 1/\sqrt{t_{obs}}$, already in the case $q = 0.5$ we should increase t_{obs} by a factor of 4 which could be somewhat problematic given the technical constraints of the SWIPE payload. On the other hand, the noise reduction is also limited by the level of systematics.

3.1.2 Frequency channel correlations

As detailed in Appendix B and according to [13, 18] correlations among different frequency channels are taken into account by specifying the *frequency coherence* $\xi_j \approx 1/\sqrt{2}\Delta\beta_j$ ($j = S, D$) which quantifies spectral variations of foregrounds across the sky, $\Delta\beta_j$ being the dispersion of the foreground spectral index β_j through the sky. Two extreme cases corresponding to no correlation and perfect correlation then arise in the limits $\xi \rightarrow 0$ and $\xi \rightarrow \infty$ respectively.

In this section we consider deviations from our fiducial value $\Delta\beta_j = 0.2$ which is consistent with findings by [16, 19, 20]. Results are summarized in Figure 7 for the combination

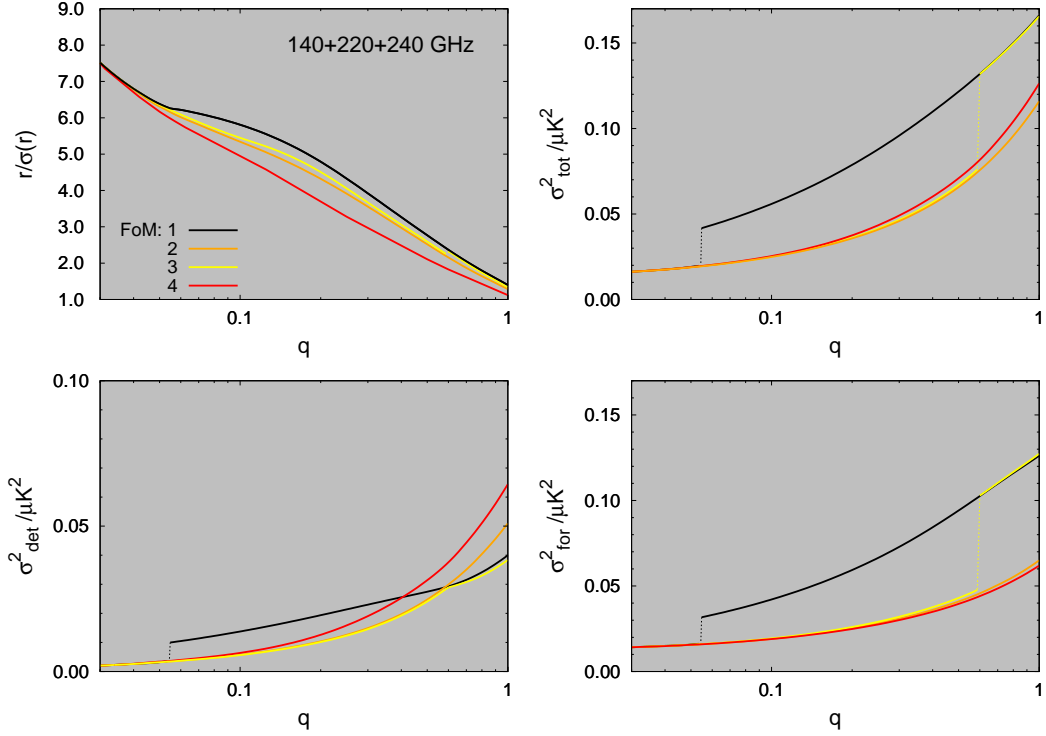


Figure 4. r/σ_r and σ_x^2 ($x = \text{tot, det, for}$) as a function of q for FoM 1–4 and SWIPE 140 + 220 + 240 GHz.

140 + 220 + 240 GHz (different combinations giving similar qualitative results). We note that configurations satisfying our FoM’s are not substantially affected by the value of $\Delta\beta_j$ (or ξ_j). Nevertheless, as expected, r/σ_r (σ_x^2) decreases (increases) as channels become less correlated (see right bottom panel of Figure 7).

3.2 High+Low frequencies

Let us now consider the high frequency combination 140 + 220 + 240 GHz and extend our analysis including the low frequency ground-based instrument (STRIP), observing at 43 and (possibly) at 90 GHz.

In its basic configuration the STRIP focal plane is supposed to consist of an array of 49 polarimeters at 43 GHz accommodated in 7 modules each including 7 detectors plus a smaller array of 6 polarimeters at 90 GHz mainly used as monitors of atmospheric emission.

Motivated by results of section 3.1 according to which the presence of a 90 GHz channel seems to substantially improve the signal to noise ratio r/σ_r , we also consider the possibility to replace n modules at 43 GHz with an equal number of 90 GHz modules each accommodating 30 detectors (here we are supposing that the detector’s dimensions simply scale as the wavelength so that 30 detectors at 90 GHz with resolution $\theta_{FWHM} = 15'$ or 7 detectors at 43 GHz with resolution $\theta_{FWHM} = 30'$ occupy the same area). A generic focal plane, therefore, will consist of $7 - n$ modules at 43 GHz plus n modules at 90 GHz for a total of $(7 - n) \times 7$ and $n \times 30$

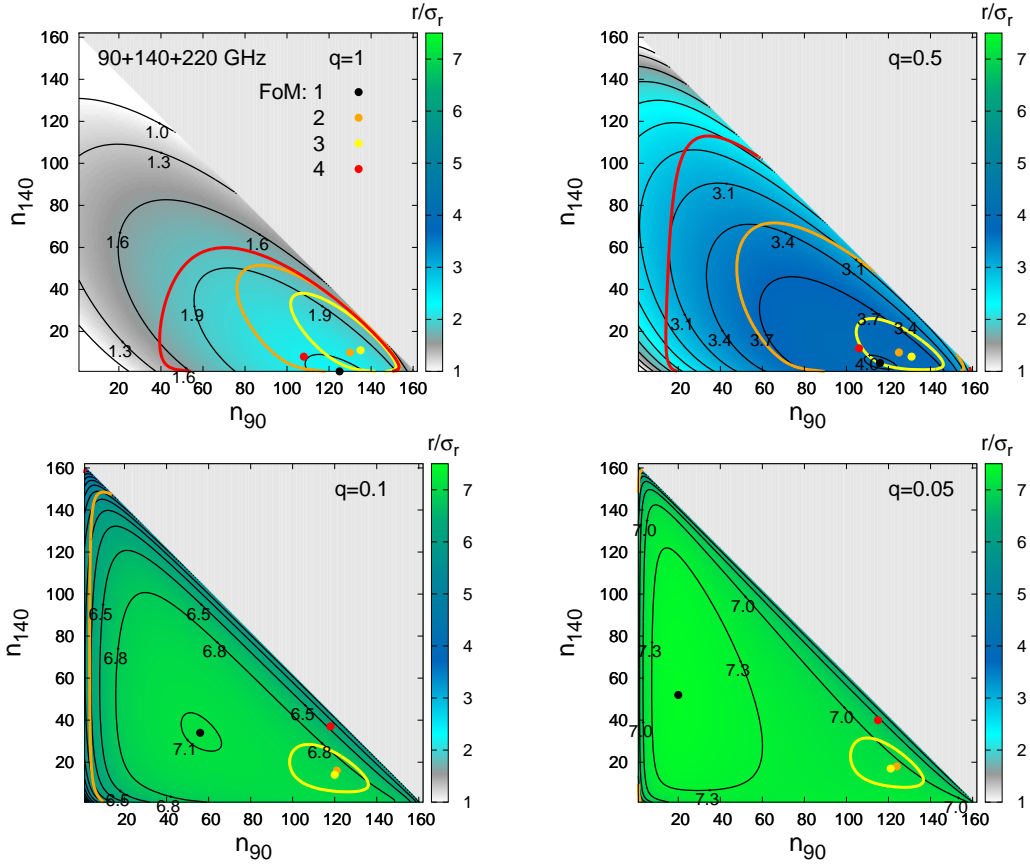


Figure 5. As Figure 3 but for SWIPE 90 + 140 + 220 GHz.

detectors respectively (plus the 6 detectors at 90 GHz with resolution $\theta_{FWHM} = 30'$ devoted to atmospheric emission).

For n fixed, we then proceed as in section 3.1 to find the configurations satisfying our FoM's. The left panel of Figure 8 shows the sensitivities σ_{pix} (rescaled to 1° pixel) of 43 and 90 GHz low frequency channels as a function of n , the number of 90 GHz modules in the focal plane. For comparison the sensitivity of the 90 GHz channel of SWIPE combination 90 + 140 + 220 GHz (FoM 1, i.e. 125 detectors \times 3 modes) is also shown. As clearly visible, this latter value is always far below the sensitivity of the STRIP 90 GHz channel meaning that, although the addition of low frequencies somewhat improve r/σ_r , this is substantially lower than the value expected from SWIPE 90 + 140 + 220 GHz (FoM 1) (see right panel of Figure 8). Figure 9 then displays configurations which satisfy FoM 1–4 for $n = 0, 1, 2, 3, 4, 5$ (green dots). In the same Figure, contours enclose configurations for which $r/\sigma_r > 1$ (top left panel) or σ_{tot}^2 , σ_{for}^2 and σ_{det}^2 deviate by no more than 5% from their minimum values (top right, bottom right and bottom left panel respectively). Results expected from SWIPE only (red) are also shown for comparison.

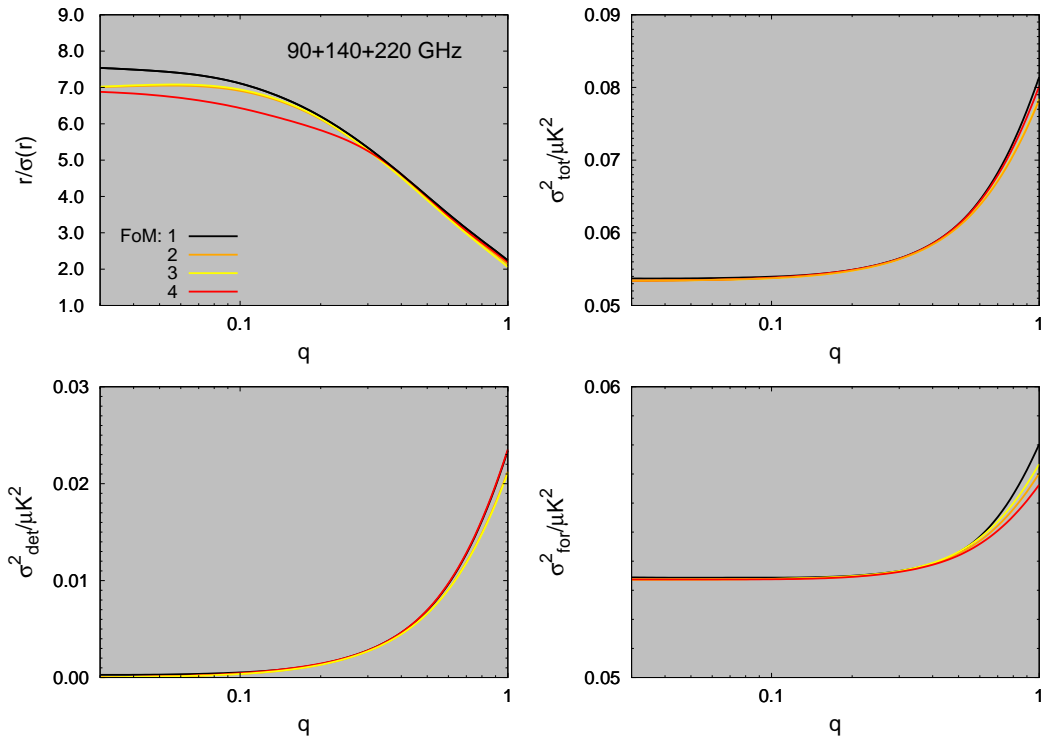


Figure 6. As Figure 4 but for SWIPE 90 + 140 + 220 GHz.

3.3 Including E -modes

In this section we investigate the effect of including E -modes in the analysis. Since E -modes should provide strong constraints on the optical depth τ , as explained in section 2, we extend the set of parameters to be explored in FM evaluations by adding τ and A_s , namely $\mathbf{p} = \{r, \tau, \ln(10^{10} A_s), \mathcal{A}_S^B, \mathcal{A}_D^B, \beta_S, \beta_D\}$, and we assume $\mathcal{A}_{S(D)}^B = 0.34(0.56)\mathcal{A}_{S(D)}^E$ according to [21]. Results are summarized in Figure 10 which shows the behavior of the signal to noise ratio r/σ_r as a function of r in the following cases satisfying FoM 1:

- SWIPE, B -modes only
- SWIPE, B - and E -modes
- SWIPE+STRIP, B - and E -modes

For SWIPE (STRIP) we consider both the combinations 90+220+240 GHz and 140+220+240 GHz (43 GHz only ($n = 0$) and 43 + 90 GHz ($n = 5$)).

As already observed in previous sections the presence of the 90 GHz high frequency channel substantially improves the precision with which r is measured. This is further enhanced by adding low frequency channels and improves as more 43 GHz modules are replaced by 90 GHz ones. The STRIP(43 + 90 GHz)+SWIPE(90 + 140 + 220 GHz) combination would then be able to measure $r \simeq 0.06$ at $3 - \sigma$ level and set upper limits if $r \lesssim 0.02$. On the other hand, if replacing the SWIPE(90 + 140 + 220 GHz) with the SWIPE(140 + 220 + 240 GHz), a $3 - \sigma$ detection is only possible for $r \simeq 0.1$. Finally, in Table 2 we give the uncertainties on

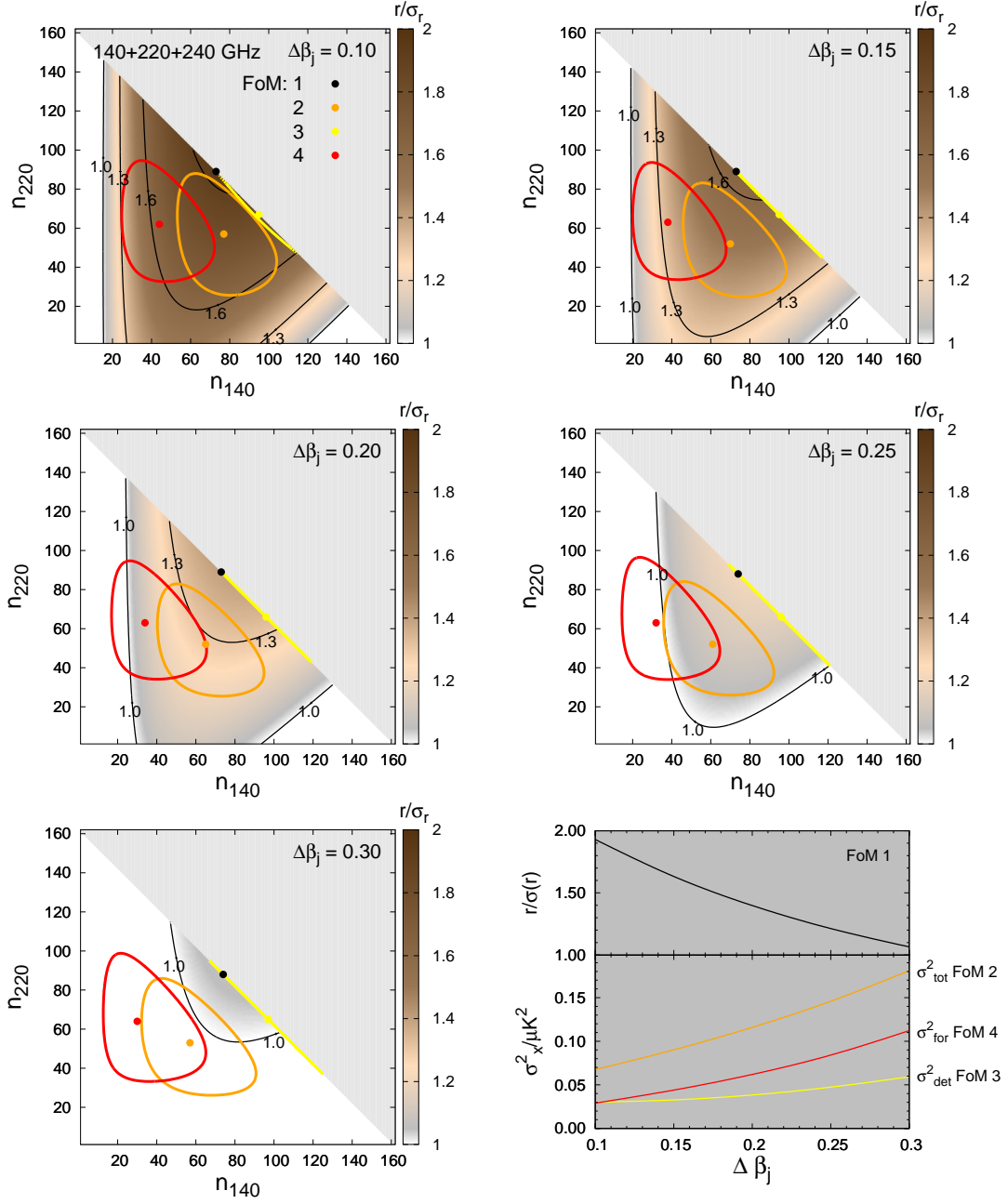


Figure 7. The effect of frequency channel correlations on focal plane configurations for SWIPE 140 + 220 + 240 GHz. Apart the different contour scale for r/σ_r , lines and colors are as in previous Figures. The right bottom panel shows r/σ_r , σ_{tot}^2 , σ_{det}^2 and σ_{for}^2 for FoM 1, 2, 3 and 4 respectively as a function of the *frequency coherence* $\xi_j \approx 1/\sqrt{2}\Delta\beta_j$ ($j = S, D$).

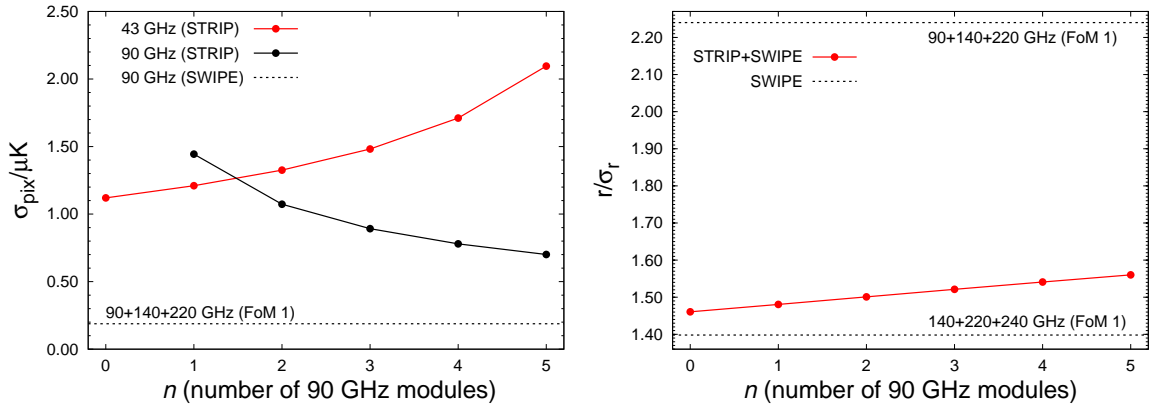


Figure 8. *Left panel:* sensitivity of STRIP 43 GHz and 90 GHz channels as a function of n , the number of 90 GHz modules in the focal plane (see text). *Right panel:* r/σ_r as a function of n for the STRIP(43+90 GHz)+SWIPE(140+220+240 GHz) combination.

SWIPE 140+220+240 GHz ($E + B$)		
	σ_τ	$\sigma_{\ln(10^{10}A_s)}$
SWIPE	0.023	0.054
STRIP+SWIPE ($n = 0$)	0.022	0.051
STRIP+SWIPE ($n = 5$)	0.014	0.039

SWIPE 90+140+220 GHz ($E + B$)		
	σ_τ	$\sigma_{\ln(10^{10}A_s)}$
SWIPE	0.019	0.046
STRIP+SWIPE ($n = 0$)	0.013	0.036
STRIP+SWIPE ($n = 5$)	0.013	0.036

Table 2. Uncertainties on τ and $\ln(10^{10}A_s)$ for different cases considered in the text. Note that σ_τ and $\sigma_{\ln(10^{10}A_s)}$ do not depend on the value of r .

τ and $\ln(10^{10}A_s)$ which turn out to be competitive with the current ones, these latter being $\sigma_\tau = 0.017$ and $\sigma_{\ln(10^{10}A_s)} = 0.034$ [14].

4 Conclusions

In this work we have performed optimization and forecasting analysis for LSPE experiment aimed to CMB B -modes measurements. To this aim we have investigated various configurations of the focal plane obtained by considering different combinations of frequency channels and/or varying the number of detectors within each channel (keeping their total number fixed). Four Figures of Merit (FoM), based on the forecasted uncertainty σ_τ of the tensor-to-scalar ratio r and the expected map variance from foreground and instrumental noise residuals, were then defined in order to identify optimal focal planes (see Section 3.1).

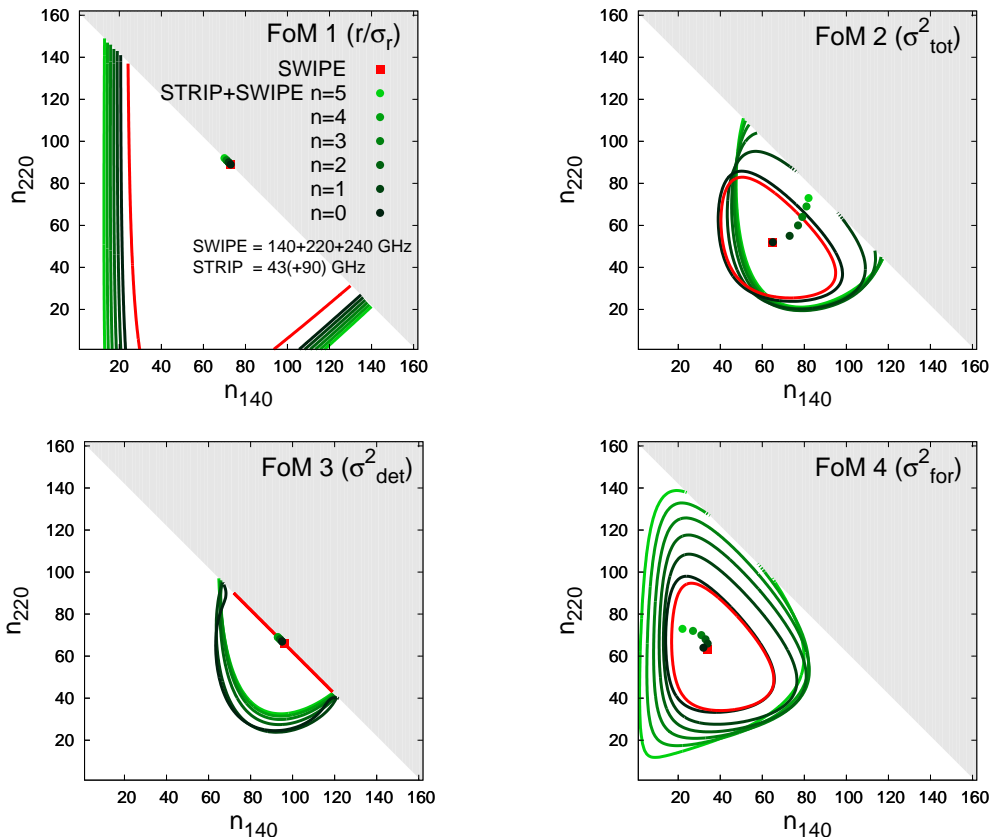


Figure 9. STRIP+SWIPE configurations satisfying FoM 1–4 for $n = 0, 1, 2, 3, 4, 5$ (green dots). Contours enclose configurations for which $r/\sigma_r > 1$ (top left panel) or σ_{tot}^2 , σ_{for}^2 and σ_{det}^2 deviate by no more than 5% from their minimum values (top right, bottom right and bottom left panel respectively). Results expected from SWIPE only (red) are also shown for comparison.

For the balloon-borne high frequency instrument SWIPE, we considered a combination of 3 frequencies, chosen among 90, 140, 220 and 240 GHz. On the other hand, the low frequency one, STRIP, was assumed to consist of 2 channels at 43 and 90 GHz.

We found that the presence of the high frequency 90 GHz channel substantially improve the precision on r (by a 40 – 60% depending on the details of the configurations). Nevertheless, given the impossibility to accommodate large size detectors into the focal plane and the aperture constraints for the SWIPE telescope, such 90 GHz detectors would not comply with the baseline requirement of maintaining a higher number of modes per detector, which was originally chosen for the focal plane design of SWIPE. Therefore, the 140+220+240 GHz high frequency combination turns out to be the preferred one. In this case, however, the configuration which provides the higher signal to noise r/σ_r is quite different from the one yielding the lower variance from non-cosmic signal (see e.g. Table 1 and Figure 1, FoM 1 compared to FoM 2 and 3) so that a possible compromise between the two should be considered.

Constraints on r are somewhat improved if high frequency measurements are comple-

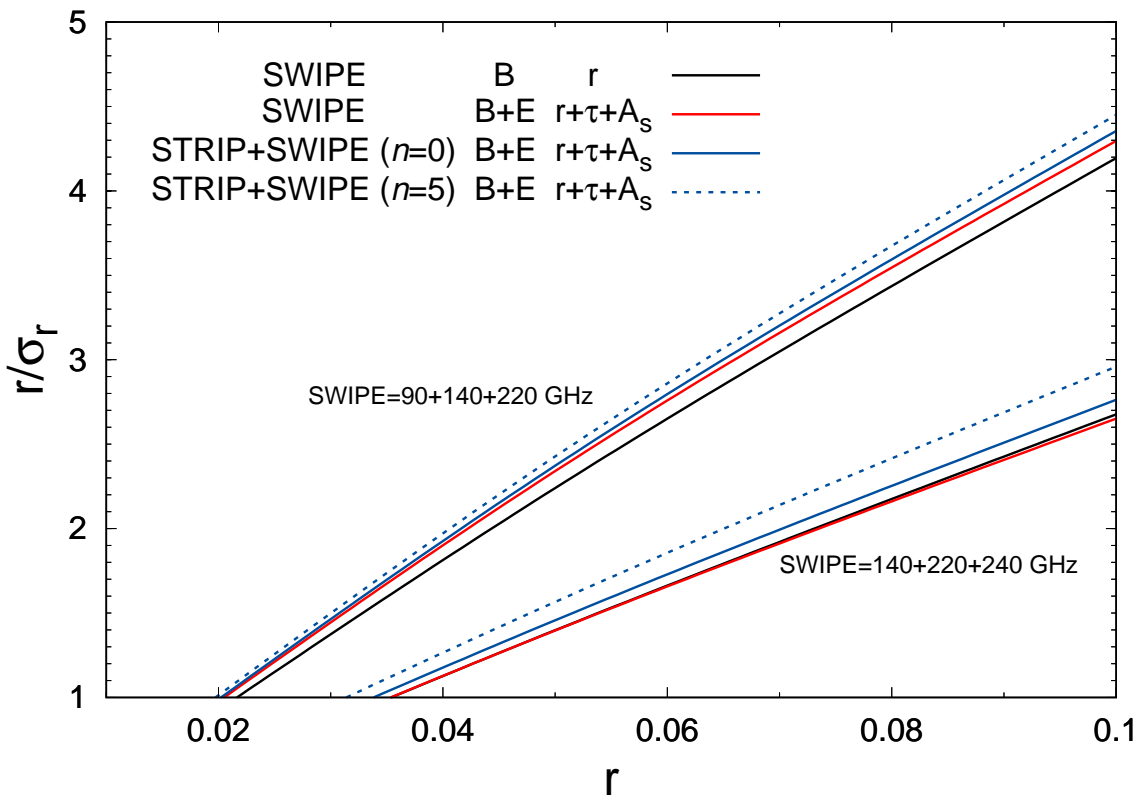


Figure 10. r/σ_r as a function of r for SWIPE (B -modes only), SWIPE ($B + E$ -modes) and SWIPE+STRIP ($B + E$ -modes). Results are given for FoM 1 and different frequency channel combinations.

mented by 43 GHz low frequency ones and are further enhanced as more as 43 GHz detectors are replaced by 90 GHz (low frequency) ones. Effects of reducing the instrumental noise (e.g. by increasing the observation time) are also discussed in Section 3.1.1.

We, however, advise the reader that, because of the issues and limitations (described at the end of Section 2) due to our simplified procedure, our findings should be considered as indicative of the need for more investigation to be performed through realistic simulations of the sky to which apply foreground separation/cleaning procedures.

Although only indicative, our results could however be of some interest for the design of LSPE-like experiments.

A Foreground removal

In order to perform our analysis and include the effect of foregrounds in the Fisher Matrix formalism, we follow the method described in [13] which permits to minimize the non-cosmic signal (instrumental noise and foreground contaminations) by taking a suitable linear combination of sky maps observed at different frequencies. For each focal plane configuration, the final result is two cleaned polarization maps (E - and B -modes) which are unbiased and have the smallest rms errors from instrumental noise and foregrounds combined. Here below,

we briefly review the main results of the procedure while refer the reader to [13] for more technical details.

Let us suppose a multifrequency experiment measuring E and B and let n_ν^X be the number of frequency channels with which $X = E, B$ is observed. The spherical harmonic coefficients observed at the frequency ν will then be:

$$a_{lm}^{X\nu} = c_{lm}^X + r_{lm}^{X\nu} \quad (\text{A.1})$$

where c_{lm}^X is the (frequency independent) CMB signal and $r_{lm}^{X\nu} = n_{lm}^{X\nu} + \sum_j f_{lm,j}^{X\nu}$ includes the instrumental noise $n_{lm}^{X\nu}$ and the possible contribution of j different foregrounds $f_{lm,j}^{X\nu}$. In vector notation we can write:

$$\mathbf{a}_{lm} = \begin{bmatrix} \mathbf{a}_{lm}^E \\ \mathbf{a}_{lm}^B \end{bmatrix} \quad \mathbf{c}_{lm} = \mathbf{A} \begin{bmatrix} c_{lm}^E \\ c_{lm}^B \end{bmatrix} \quad \mathbf{r}_{lm} = \begin{bmatrix} \mathbf{r}_{lm}^E \\ \mathbf{r}_{lm}^B \end{bmatrix}$$

$$\mathbf{a}_{lm} = \mathbf{c}_{lm} + \mathbf{r}_{lm} \quad (\text{A.2})$$

where \mathbf{a}_{lm} , \mathbf{c}_{lm} and \mathbf{r}_{lm} are vectors of length $n_\nu = n_\nu^E + n_\nu^B$, the entries of \mathbf{a}_{lm}^X (\mathbf{r}_{lm}^X) are the n_ν^X measured harmonic coefficients $a_{lm}^{X\nu}$ ($r_{lm}^{X\nu}$) given by eq. (A.1) and the $n_\nu \times 2$ scan matrix \mathbf{A} is given by:

$$\mathbf{A} = \begin{bmatrix} \mathbf{e}^E & \mathbf{0} \\ \mathbf{0} & \mathbf{e}^B \end{bmatrix} \quad (\text{A.3})$$

(\mathbf{e}^X being the n_ν^X -dimensional column vector consisting of ones).

We can then define the angular auto- and cross-power spectra of CMB polarization, detector noise and foregrounds:

$$\begin{aligned} \langle c_{lm}^{X*} c_{l'm'}^{X'} \rangle &= C_l^X \delta_{ll'} \delta_{mm'} \delta_{XX'} \\ \langle n_{lm}^{X\nu*} n_{l'm'}^{X'\nu'} \rangle &= N_l^{X\nu\nu'} \delta_{ll'} \delta_{mm'} \delta_{XX'} \delta_{\nu\nu'} \\ \langle f_{lmj}^{X\nu*} f_{l'm'j'}^{X'\nu'} \rangle &= F_{lj}^{X\nu\nu'} \delta_{ll'} \delta_{mm'} \delta_{XX'} \delta_{jj'} \end{aligned} \quad (\text{A.4})$$

and the $n_\nu \times n_\nu$ total covariance matrix \mathbf{R}_l of the non-cosmic signal (detector noise and foregrounds):

$$\mathbf{R}_l = \begin{bmatrix} \mathbf{R}_l^E & \mathbf{0} \\ \mathbf{0} & \mathbf{R}_l^B \end{bmatrix} \quad (\text{A.5})$$

built by the two $n_\nu^X \times n_\nu^X$ covariance matrices \mathbf{R}_l^X specifying the correlation of the non-cosmic signal among different frequency channels. Their components read:

$$\left[\mathbf{R}_l^X \right]_{ab} = \left[\mathbf{N}_l^X \right]_{ab} + \left[\mathbf{F}_l^X \right]_{ab} = N_l^{X\nu_a\nu_a} \delta_{ab} + \sum_j F_{lj}^{X\nu_a\nu_b}$$

(here $a, b = 1, \dots, n_\nu^X$ while ν_a denotes the a -th frequency at which X is observed; \mathbf{N}_l^X and \mathbf{F}_l^X are the covariance matrices of detector noise and foregrounds respectively). Note that, here above, we have assumed that: i) CMB, instrumental noise and different foregrounds are all uncorrelated with each other, i.e. $\langle c_{lm}^{X\nu*} n_{l'm'}^{X'\nu'} \rangle = \langle c_{lm}^{X\nu*} f_{l'm',j}^{X'\nu'} \rangle = \langle f_{lm,j}^{X\nu*} n_{l'm'}^{X'\nu'} \rangle = 0$; ii) the vanishing of the cross-correlations between B -modes and E -modes due to symmetry reasons holds also for foregrounds; iii) as usual, instrumental noise introduces no cross-correlation among E and B as well as among different frequency channels.

Let us now consider the linear combination $\mathbf{a}_{lm} = \mathbf{W}_l^t \mathbf{a}_{lm}$ (t denoting the transpose matrix) of sky maps observed at different frequencies. If we require that $\mathbf{W}_l^t \mathbf{A} = \mathbf{I}$ the two resulting maps (E, B) may be written as:

$$\mathbf{a}_{lm} = \mathbf{c}_{lm} + \mathbf{r}_{lm} \quad (\text{A.6})$$

where:

$$\mathbf{a}_{lm} = \begin{bmatrix} a_{lm}^E \\ a_{lm}^B \end{bmatrix} \quad \mathbf{c}_{lm} = \begin{bmatrix} c_{lm}^E \\ c_{lm}^B \end{bmatrix} \quad \mathbf{r}_{lm} = \mathbf{W}_l^t \mathbf{r}_{lm} = \begin{bmatrix} r_{lm}^E \\ r_{lm}^B \end{bmatrix} \quad (\text{A.7})$$

Thus, since the CMB signal does not depend on the frequency, it is untouched regardless of the chosen \mathbf{W}_l , while this latter may be chosen to suppress the impact of the non-cosmic signal. The variance of the resulting maps is then minimized provided that the $n_\nu \times 2$ weighting matrix \mathbf{W}_l has the form (see [13]):

$$\mathbf{W}_l = \mathbf{R}_l^{-1} \mathbf{A} (\mathbf{A}^t \mathbf{R}_l^{-1} \mathbf{A})^{-1} \quad (\text{A.8})$$

Eqs. (A.7) and (A.8) thus gives the spherical harmonic coefficients of the two cleaned maps. In particular, \mathbf{r}_{lm} gives the residual non-cosmic signal after the cleaning procedure. Its (2×2) covariance matrix:

$$\mathbf{R}_l = (\mathbf{A}^t \mathbf{R}_l^{-1} \mathbf{A})^{-1} = \mathbf{W}_l^t \mathbf{R}_l \mathbf{W}_l = \begin{bmatrix} \mathbf{R}_l^E & 0 \\ 0 & \mathbf{R}_l^B \end{bmatrix} \quad (\text{A.9})$$

provides the angular power spectra $\mathbf{R}_l^X = \mathbf{N}_l^X + \mathbf{F}_l^X$ of residual detector noise and foregrounds in the cleaned maps needed to implement the Fisher matrix approach of Sec. 2 (see eq. (2.2)).

B Foreground models

In order to implement our forecasting method, foreground angular power spectra should be properly modelled and, in this respect, we rely on recent measurements provided by the Planck Collaboration [16, 21, 22].

Of all diffuse galactic foregrounds, dust (D) and synchrotron (S) are the relevant ones for polarization measurements. Angular power spectra for $j = D, S$ are modeled as:

$$F_{lj}^{X\nu\nu'} = \mathcal{A}_j^X \Theta_{lj}^X \mathcal{F}_j^\nu \mathcal{F}_j^{\nu'} \mathcal{R}_j^{\nu\nu'} \quad (\text{B.1})$$

Here, \mathcal{A}_j^X is the overall amplitude and spectra have been factorized into a multipole dependence term Θ_{lj}^X , a frequency dependence term \mathcal{F}_j^ν and a frequency correlation term $\mathcal{R}_j^{\nu\nu'}$ which, following [13, 18], we assume to be modelled as:

$$\mathcal{R}_j^{\nu\nu'} \simeq e^{-\frac{1}{2} \left[\frac{\ln(\nu/\nu')}{\xi_j} \right]^2} \quad (\text{B.2})$$

where the *frequency coherence* ξ_j accounts for slight variations of the frequency dependence of foregrounds across the sky. It determines how many powers of e we can change the frequency before the correlation between the channels starts to break down. The two limits $\xi \rightarrow 0$ and $\xi \rightarrow \infty$ correspond to the two extreme cases of no correlation and perfect correlation respectively. Real foregrounds typically have behaviours that are intermediate between these two. In [18] it is shown that for a spectrum $\propto f(\nu)\nu^\beta$ ($f(\nu)$ being some arbitrary function)

Synchrotron		
$\mathcal{A}_S^E = 0.0031 \mu\text{K}$	$\Theta_{lD}^X = \left(\frac{l}{l_0}\right)^{\alpha^X}$	$\mathcal{F}_S^\nu = \left(\frac{\nu}{\nu_0}\right)^{\beta_S} \frac{g_\nu}{g_{\nu_0}}$
$\mathcal{A}_S^B = 0.35\mathcal{A}_S^E$	$\alpha^E = -2.49$	$\beta_S = -3.14$
	$\alpha^B = -2.32$	$\nu_0 = 30 \text{ GHz}$
	$l_0 = 80$	
Thermal Dust		
$\mathcal{A}_D^E = 0.2765 \mu\text{K}$	$\Theta_{lD}^X = \left(\frac{l}{l_0}\right)^{\alpha^X}$	$\mathcal{F}_D^\nu = \left(\frac{\nu}{\nu_0}\right)^{\beta_D+1} \frac{B_{\nu_0}}{B_\nu} \frac{g_\nu}{g_{\nu_0}}$
$\mathcal{A}_D^B = 0.56\mathcal{A}_D^E$	$\alpha^E = -2.53$	$\beta_D = 1.59$
	$\alpha^B = -2.62$	$\nu_0 = 353 \text{ GHz}$
	$l_0 = 80$	$B_\nu = e^{\frac{h\nu}{kT_D}} - 1$
		$T_D = 19.6 \text{ K}$

Table 3. Specifications of foreground model. Here $g_\nu = (e^x - 1)^2/x^2 e^x$, where $x = h\nu/kT_{CMB}$, accounts for the conversion from antenna to thermodynamic temperature.

we have $\xi \approx 1/\sqrt{2}\Delta\beta$ where $\Delta\beta$ is the rms dispersion across the sky of the spectral index β . For simplicity we assume as fiducial value $\Delta\beta = 0.2$ for both S and D according to the findings by [16, 19, 20].

Specifications of foreground models are summarized in Table 3. Galactic foregrounds amplitudes, $\mathcal{A}_{D(S)}^X$, are the mean values evaluated by Planck [21] with 2° FWHM apodization over an effective sky fraction $f_{sky} = 0.68$. We assume these values to hold also in the region observed by LSPE. Finally, FM is evaluated by adopting the following Gaussian priors:

$$\frac{\sigma_P(\mathcal{A}_S^B)}{\mathcal{A}_S^B} = 0.18, \quad \sigma_P(\beta_S) = 0.04, \quad \frac{\sigma_P(\mathcal{A}_D^B)}{\mathcal{A}_D^B} = 0.02, \quad \sigma_P(\beta_D) = 0.02$$

which correspond to $\approx 1 - \sigma$ errors as reported by [16, 19, 21].

C Instrumental noise

Assuming the instrumental noise is white and Gaussian, the noise angular power spectrum for $X = E, B$ reads:

$$N_l^{X\nu} = \sigma_{pix}^2 \Omega_{pix} e^{l(l+1)\sigma_B^2} \quad (\text{C.1})$$

where σ_{pix} and $\Omega_{pix} = \theta_{FWHM}^2$ are the pixel noise and area respectively, θ_{FWHM} is the full width at half maximum beamsize and $\sigma_B = \theta_{FWHM}/\sqrt{8 \ln 2}$. These quantities depends on the features of the detectors and are summarized in Table 4.

Note that, for simplicity, we have assumed the detectors to have Gaussian beam profiles that is not the case with the multimode detectors of SWIPE. Sensitivities in Table 4 are however calculated on the base of realistic multimode throughputs.

	STRIP		SWIPE			
ν/GHz	43	90	90	140	220	240
$\theta_{FWHM}/\text{arcmin}$	30.00	15.00 ^b	85.95	85.95	85.95	85.95
$\sigma_{pix}/\mu\text{K}$ E, B ^a	7.84	8.78	2.10	1.35	5.51	11.47
Observing time	1 year		14 days			
Duty cycle (%)	35		100			
f_{sky}	0.20		0.20			

^a σ_{pix} is the sensitivity per 1° pixel per detector

^b $\theta_{FWHM} = 30$ arcmin for the 6 detectors aimed at monitoring the atmospheric emission (see text)

Table 4. Characteristics of LSPE instruments.

D Angular power spectra covariance matrix

Given the binned angular power spectra D_B^X ($X = E, B$) as defined in (2.1) and (2.2):

$$D_B^X = \frac{1}{\Delta l} \sum_{l \in b} D_l^X \quad D_l^X = \frac{l(l+1)}{2\pi} (C_l^X + R_l^X) \quad (\text{D.1})$$

their covariance matrix \mathbf{D}_b reads:

$$\mathbf{D}_b = \sum_{l \in b} \frac{2}{(2l+1)f_{sky}\Delta l^2} \begin{bmatrix} (D_l^E)^2 & 0 \\ 0 & (D_l^B)^2 \end{bmatrix} \quad (\text{D.2})$$

where f_{sky} is the observed sky fraction.

Acknowledgments

Authors wish to thank Paolo de Bernardis for many useful insights. This work is supported by ASI (Agenzia Spaziale Italiana) under contract ASI I/022/11/0 "Large Scale Polarization Explorer (LSPE)".

References

- [1] BICEP2 Collaboration, Keck Array Collaboration, Ade, P. A. R., et al. 2016, *Physical Review Letters*, 116, 031302
- [2] Buzzelli, A., de Gasperis, G., de Bernardis, P., Masi, S., & Vittorio, N. 2017, *Optimization of the half wave plate configuration for the LSPE-SWIPE experiment*, *Journal of Physics Conference Series*, 841, 012001
- [3] Gualtieri, R., Battistelli, E. S., Cruciani, A., et al. 2016, *Multi-mode TES Bolometer Optimization for the LSPE-SWIPE Instrument*, *Journal of Low Temperature Physics*, 184, 527
- [4] De Matteis, M., De Blasi, M., Vallicelli, E. A., et al. 2017, *A CMOS application-specified-integrated-circuit for 40 GHz high-electron-mobility-transistors automatic biasing*, *Review of Scientific Instruments*, 88, 024702
- [5] Bersanelli, M., Mennella, A., Morgante, G., et al. 2012, *A coherent polarimeter array for the Large Scale Polarization Explorer (LSPE) balloon experiment*, *Proc. SPIE*, 8446, 84467C

- [6] Aiola, S., Amico, G., Battaglia, P., et al. 2012, *The Large-Scale Polarization Explorer (LSPE)*, Proc. SPIE, 8446, 84467A
- [7] de Bernardis, P., Aiola, S., Amico, G., et al. 2012, *SWIPE: a bolometric polarimeter for the Large-Scale Polarization Explorer*, Proc. SPIE, 8452, 84523F
- [8] Errard, J., Stivoli, F., & Stompor, R. 2011, *Framework for performance forecasting and optimization of CMB B-mode observations in the presence of astrophysical foregrounds*, Phys. Rev. D, 84, 063005
- [9] Mainini, R. & Gervasi, M. 2017, *Constraining inflationary parameters with the Large Scale Polarization Explorer (LSPE)*, in preparation
- [10] Spinelli, S., Fabbian, G., Tartari, A., et al. 2011, *A template of atmospheric O₂ circularly polarized emission for cosmic microwave background experiments*, Mon. Not. R. Astron. Soc., 414, 3272
- [11] Battistelli, E. S., Amico, G., Baú, A., et al. 2012, *Intensity and polarization of the atmospheric emission at millimetric wavelengths at Dome Concordia*, Mon. Not. R. Astron. Soc. 423, 1293
- [12] Mainini, R., Minelli, D., Gervasi, M., et al. 2013, *An improved upper limit to the CMB circular polarization at large angular scales*, J. Cosmology Astropart. Phys., 8, 033
- [13] Tegmark, M., Eisenstein, D. J., Hu, W., & de Oliveira-Costa, A. 2000, *Foregrounds and Forecasts for the Cosmic Microwave Background*, ApJ, 530, 133
- [14] Planck Collaboration, Planck 2015 results XIII, 2016, A&A, 594, A13
- [15] Amarie, M., Hirata, C., & Seljak, U. 2005, *Detectability of tensor modes in the presence of foregrounds*, Phys. Rev. D, 72, 123006
- [16] Planck Collaboration, Planck Intermediate Results XXII, 2015 A&A576, A107
- [17] Choi S.K. & Page, L.A. 2015, *Polarized galactic synchrotron and dust emission and their correlation*, JCAP, 12, 020
- [18] Tegmark, M. 1998, *Removing Real-World Foregrounds from Cosmic Microwave Background Maps*, ApJ, 502, 1
- [19] Fuskeland U., Wehus I. K., Eriksen H. K., Næss S. K. 2014, *Spatial Variations in the Spectral Index of Polarized Synchrotron Emission in the 9 yr WMAP Sky Maps*, ApJ, 790, 104
- [20] Krachmalnicoff N., Baccigalupi C., Aumont J., Bersanelli M., Mennella A. 2016, *Characterization of foreground emission on degree angular scales for CMB B-mode observations. Thermal dust and synchrotron signal from Planck and WMAP data*, A&A588, A65
- [21] Planck Collaboration, Planck 2015 Results X, 2016, A&A, 594, A10
- [22] Planck Collaboration, Planck Intermediate Results XXX, 2016, A&A, 586, A133